Strain Rate Effect and Mechanical Constitutive Model of Coal Samples Under Dynamic Load

Zhoujie Gu,[1,2] Rongxi Shen,[1,2,3] Zhentang Liu,[1,2] Xin Zhou,[1,2] Xiaoliang Li,[1,2] Zesheng Zang,[1,2] Li Zhang,[1,2] Wei Liu,[1,2] and Xi Wang[1,2]

The failure characteristics and mechanism of coal under dynamic and static loading are a basic problem for studying the mechanism of rock burst. It is also a basic research problem to solve the protection of deep underground engineering. By using the split Hopkinson bar system, the mechanical behavior and energy change of coal were analyzed. The law of stress and energy evolution during coal sample failure were analyzed. Combined with a high-speed camera, the analysis of a coal sample after failure showed that, in the process of dynamic loading, it produced cracks along its axial direction. The critical strain rate in the dynamic damage process of coal samples was also analyzed, and the damage degree of coal samples intensified gradually within a certain range of strain rate. Finally, a dynamic mechanical constitutive model was established by considering the influence of strain rate, and the damage changes of coal samples were analyzed. The research results provide a reference basis for further revealing the mechanism of rock burst and preventing coal rock dynamic disaster.

KEY WORDS: Strain rate, Energy, Failure, Constitutive equation.

INTRODUCTION

Coal is one of the main energy sources in the world. With increasing mining depth (Kaiser et al., 2015; Fairhurst et al., 2017; Xie et al., 2019, 2021), coal and rock dynamic disasters have become increasingly serious, resulting in dynamic phenomena such as rock burst or coal and gas outburst, which seriously threatens the safety and production efficiency of mines (Xie et al., 2019; Hao et al., 2020; Li et al., 2023a). In underground coal mining, dy-namic load is produced due to roof caving, blasting or fault sliding, which has great influence on coal pillars. Therefore, the study of coal mechanical behavior and failure characteristics under dynamic load has important theoretical guidance and practical significance to analyze and prevent coal rock dynamic disaster in deep coal mining.

Scholars have conducted extensive studies on the mechanical behavior of coal under quasi-static conditions in the laboratory, including uniaxial (Liu et al., 2015; Ding et al., 2023), biaxial (Zhang et al., 2017) and true triaxial (Liu et al., 2019; Zhou et al., 2023) servo press experiments. According to some research results, the loading strain rate of samples in the above related studies is generally less than $0/s^{-1}$. However, the dynamic impact load on a sample can achieve a strain rate as high as $0–1000/s^{-1}$, which makes the dynamic failure of coal and rock instan-

---
[1]Key Laboratory of Gas and Fire Control for Coal Mines, Ministry of Education, China University of Mining and Technology, Xuzhou 221116, China.
[2]School of Safety Engineering, China University of Mining and Technology, Xuzhou 221116, China.
[3]To whom correspondence should be addressed; e-mail: shenrongxi@126.com

taneous. This also suggests that the development of most static experiments is a slow process for single loading of coal samples relative to a dynamic shock previously. Considering the time response, failure degree and other conditions, the mechanical properties of coal samples under different strain rates are quite different. In the practical application of coal mine engineering, there are a lot of damages under high strain rate, such as, among others, blasting, coal explosion and drilling operation. Compared with static loading, dynamic loading failure of coal is more consistent with the actual situation of underground coal mine (Li et al., 2008; Zhao et al., 2014; Feng et al., 2016; Gu et al., 2023). Therefore, researchers have gradually used the split Hopkinson bar (SHPB) system to test the failure behavior of coal rock under dynamic load, and have made great progress in dynamic impact mechanics. The SHPB system was mostly applied to rock materials (Li et al., 2008, 2021a; Wang et al., 2016; Yao et al., 2017; Ma et al., 2021), and then transited gradually to coal SHPB impact experiment. Scholars studied the mechanical behavior of coal under impact load (Feng et al., 2018; Li et al., 2021b), failure characteristics (Feng et al., 2020; Hao et al., 2020), microscopic characteristics (Li et al., 2020a, 2020b) and acoustic and electric response process of coal under impact (Ju et al., 2007; Yang et al., 2019; Feng et al., 2022). Although the relevant research and analysis of various indicators and parameters of coal under impact have been carried out, the relationship between stress and energy evolution in the process of coal sample crushing under dynamic load is still unclear, and the quantitative characterization and microscopic analysis of particle size distribution in coal sample crushing process are seldom studied. There are also few researches on the strength statistical damage constitutive model describing the dynamic characteristics of coal, which can be further discussed.

In this study, the relationship between stress and energy evolution in the process of coal sample crushing was analyzed in combination with high-speed photography technology. The particle size distribution and fracture mechanism of coal samples were characterized quantitatively by using scanning electron microscopy (SEM) and the fractal theory. The critical strain rate of coal sample failure during dynamic impact is also discussed. The dynamic mechanical constitutive model of coal sample was established, and the damage evolution law of coal sample was analyzed under the premise of considering strain rate. The research results provide a theoretical basis for the prevention and control of coal and rock dynamic disasters.

EXPERIMENT

Experiment System

Figure 1a shows the experimental device of SHPB, which is composed mainly of dynamic and static load loading subsystem, data acquisition subsystem, infrared velocity measurement subsystem and pressure bar main body. The dynamic and static loading subsystems are composed of bullet, incident bar and transmission bar. All the bars are made of 30Crmosini2a steel, with elastic modulus of 210 GPa and p-wave propagation velocity of 5.1 km/s.

The coal samples (Fig. 1b) used in this test came from Shandong Province, China. The size of each sample was about $\varphi 100$ mm $\times$ 50 mm. After grinding, the parallelism of both ends of a sample was controlled within the tolerance range of 0.02 mm. The wave velocity of a sample was tested in advance and samples with similar densities were selected for the test. The average mass and density of the cake samples were 516.7 g and 1.316 g/cm^3.

For the high-speed camera device (Fig. 1c), its capture frame number was set to 22,000, its photo collection interval to 45.45 μs. For the sample screening device and balance (Fig. 1d), its screen had a total of eight sizes, with maximum aperture of 45 mm and minimum aperture of 0.1 mm. Figure 1e shows the SEM images of the crushed particles of coal sample.

Test Principle and Process

As shown in Figure 2, the bullet impinges on the incident bar and forms stress wave propagation in the incident bar. The incident wave (ε_i) passes through the incident bar and acts on a coal sample to form reflected wave (ε_r) and transmitted wave (ε_t). As is the cross-sectional area of a specimen, and L is its length. A and E are the cross-sectional area and elastic modulus of the compression bar, respectively, and t is the duration of stress wave pulse. Based on the one-dimensional stress wave theory, the stress ($\sigma(t)$), average strain rate ($\dot{\varepsilon}(t)$) and strain ($\varepsilon(t)$) of the sample are deduced, respectively, as follows (Ai et al., 2019):
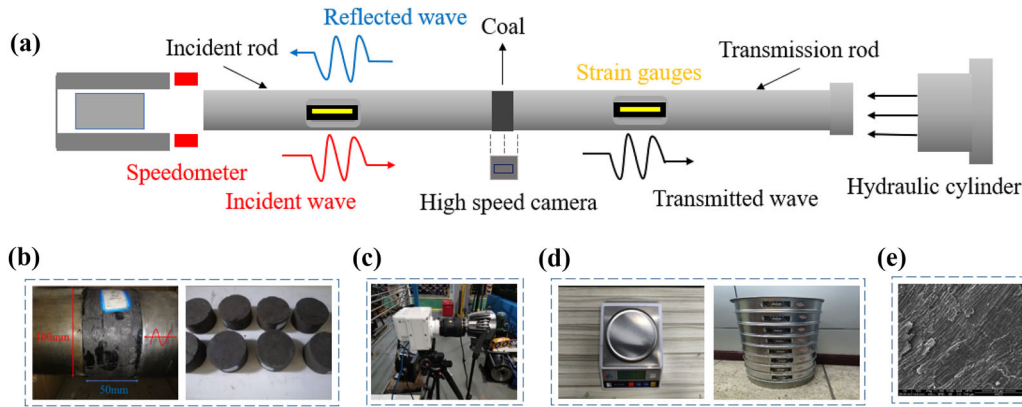
Figure 1. SPHB test equipment (**a**) Schematic diagram of SHPB test; (**b**) Coal sample; (**c**) High speed camera; (**d**) Screening and weighing; (**e**) SEM Test.
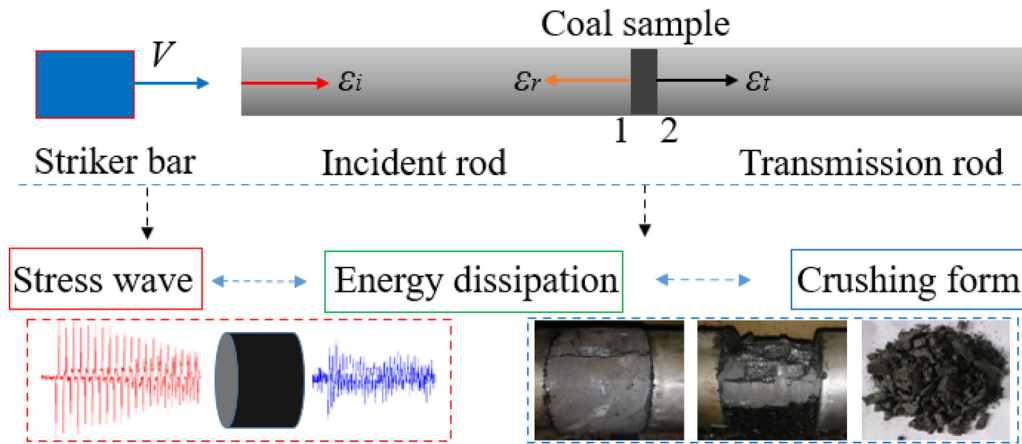

Figure 2. Experimental test schematic diagram. "1" and "2" are the two end faces of a specimen.

$$
\begin{cases}
\sigma(t) = \dfrac{A}{2A_s} E[\varepsilon_i(t) + \varepsilon_r(t) + \varepsilon_t(t)] \\[2mm]
\dot{\varepsilon}(t) = \dfrac{C}{L}[\varepsilon_i(t) - \varepsilon_r(t) - \varepsilon_t(t)] \\[2mm]
\varepsilon(t) = \dfrac{C}{L}\int_0^t [\varepsilon_i(t) - \varepsilon_r(t) - \varepsilon_t(t)]d_t
\end{cases}
\tag{1}
$$

A coal sample is tightened by loading the transmission rod, then the data acquisition system is debugged and the photography system is started synchronously. After the strain instrument is stabilized, the bullet is launched, impacting the incident rod and forming a stress wave to act on the coal sample. The coal sample is damaged or destroyed by the impact of high strain rate. Different velocities can be obtained by placing the bullet at different locations from the entry bar and then triggering the bullet with air pressure. Because the sensing distance L (mm) between the two ends of the infrared velocimeter is known, the time t (ms) of a bullet passing through the sensor can be obtained, Therefore, the impact velocity of each action on coal is quantified: $v = L/t$.

After the first impact test is completed, the stress wave data and high-speed photography images are stored. All fragments of a coal sample are collated and placed in an airtight bag for sealing storage. Then, the coal samples are screened and weighed by different sizes of screens and electronic scales. Some particles were selected for SEM analysis.

EXPERIMENTAL RESULTS

Mechanical Characteristics

The incident, reflected and transmitted waves' amplitudes increased with increase in impact velocity (Fig. 3a). The analyses show that increased impact velocity made the bullet gain more momentum to impact the incident bar, prompting the incident wave amplitude to increase. When the incident wave passed forward to the contact area of coal, the impact of the reflection spread and the transmission wave amplitude increased, but the stress wave gave priority to the reflection and this may be because the impact of time was shorter. This is also related to the material property of a sample; that is, the porous microstructure in coal. In addition, relative to the stress waveform of the rock, the wavelength of transmitted wave was larger than that of reflected wave. The interior of the coal sample was loose and porous, with many cracks. At the same time, the internal cracks of the coal sample were derived under the impact load, and the damage degree of the sample was increased.

The strain rate was positively correlated with the impact velocity (Fig. 3b). The fitting rate of this linear relationship was as high as 0.99. This shows that the experimental strain rate can be controlled by adjusting the impact velocity. The stress–strain curves of a coal sample under dynamic load (Fig. 3c) included mainly linear stage, yield stage and stress decline stage. The higher the dynamic load, the faster the initial ascent of the curve. The peak stress and strain of coal samples both showed a linear increase trend with change in dynamic load (1.06–6.25 m/s) (Fig. 3d). The linear relationship was very good: $y = av + b$ ($R^2 \geq 0.8$) within the impact velocity of 1.06–6.25 m/s.

Broken Morphology of Coal

In terms of the fracture failure form, the lumpiness scale of a coal sample failure decreased significantly (Fig. 4), indicating that there was significant correlation between failure morphology and impact velocity. When the dynamic loads on coal were 1.06 m/s and 1.99 m/s, V- or Y-type failure cracks appeared at the end face of a coal sample, but the coal samples were relatively intact and no overall crushing instability occurred. The coal samples split along the axial direction and the fragmentation degree was relatively large, mainly with large particle size when the impact velocities were 3.18 m/s, 3.97 m/s and 4.82 m/s. When the impact velocity increased to 5.51 m/s and 6.25 m/s, the coal samples broke seriously, showing tiny fragments or particles.

Energy Evolution

The incident energy $W_i(t)$, reflected energy $W_r(t)$ and transmitted energy $W_t(t)$ generated during the dynamic load impact of coal sample are defined, respectively, as (Wang et al., 2021a; Kong et al., 2022):

$$\begin{cases} W_i(t) = AEC \int\limits_0^t \varepsilon_i^2(t)d_t \\ W_r(t) = AEC \int\limits_0^t \varepsilon_r^2(t)d_t \\ W_t(t) = AEC \int\limits_0^t \varepsilon_t^2(t)d_t \end{cases} \quad (2)$$

Without considering the splashes and other related factors, the absorbed energy $W_s(t)$ during coal sample fracturing can be expressed as (Zang et al., 2021):

$$W_s(t) = W_i(t) - W_r(t) - W_t(t) \quad (3)$$

The energy dissipation rate (n) is calculated according to the total incident energy and absorbed energy, thus:

$$n = W_s(t)/W_i(t) \quad (4)$$

The energy values of each item were approximately zero at the beginning and then increase gradually with increase in time (Fig. 5a). In the end, the gradual energy curves remained constant. However, the time history curves of incident energy and reflected energy increased synchronously and varied greatly, while the transmitted energy was relatively small. Regarding the relationship between each energy value and impact velocity (Fig. 5b), all energy values increased with impact velocity. The reflected energy, transmitted energy and absorbed energy increased linearly with the incident energy (Fig. 5c–e), conforming to the linear fitting formula: $y = ax + b$ ($R^2 \geq 0.85$). In the process of impact
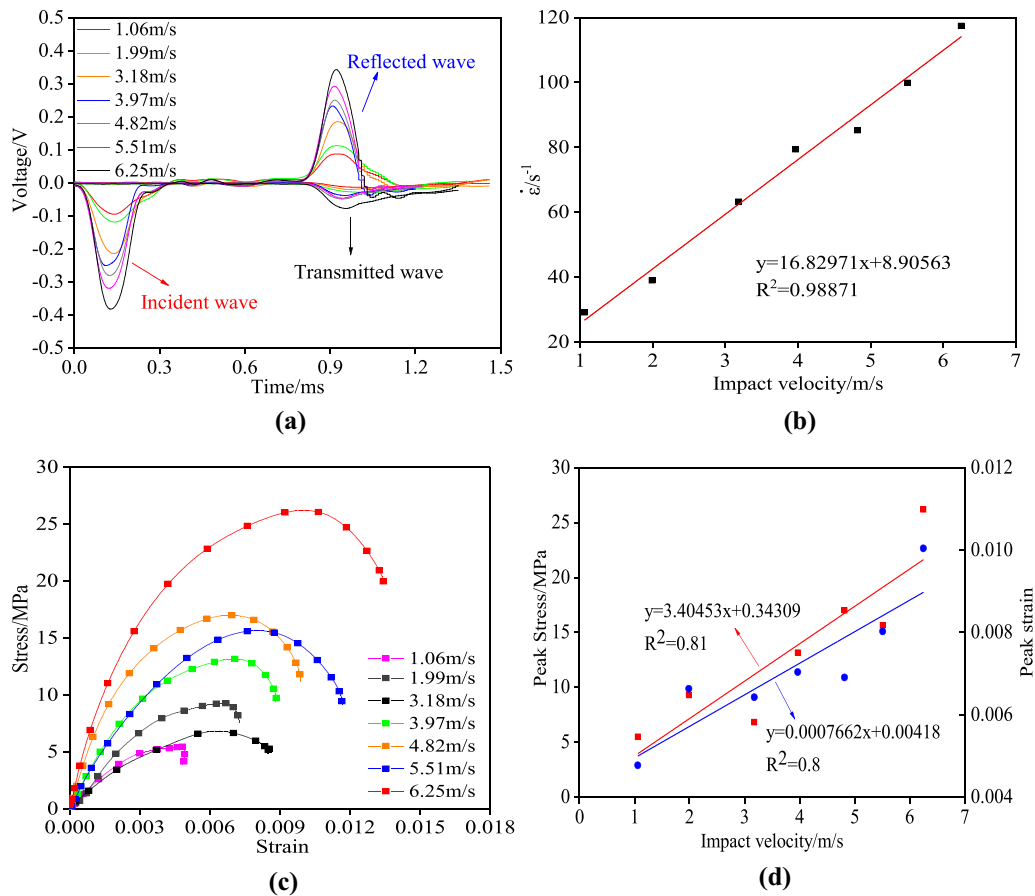
Figure 3. Mechanical characteristics of coal samples: (**a**) stress wave curve; (**b**) dynamic curve; (**c**) variation of stress and strain; (**d**) variation of peak stress and impact velocity.

Figure 4. Macroscopic failure morphology of the sample.

failure, the energy absorbed by the macroscopic crushing of coal accounted for about 15–30% of the incident energy and most of the energy was absorbed by the incident rod (Fig. 5f). The energy absorption rate still had a trend of increasing gradually from the speed of 3.18 m/s to 6.25 m/s when the coal sample failure at this stage was not complete because the low impact velocities of 1.06 m/s and 1.99 m/s were not taken into account.

ANALYSIS

Law of Stress and Energy Evolution

The energy consumption was analyzed in combination with the stress–time variation process (Fig. 6). For example, in the initial phase of AB, the coal sample was rich in pores and microcracks, and the coal sample was compressed quickly in a very short time, and the stress increased slightly, but
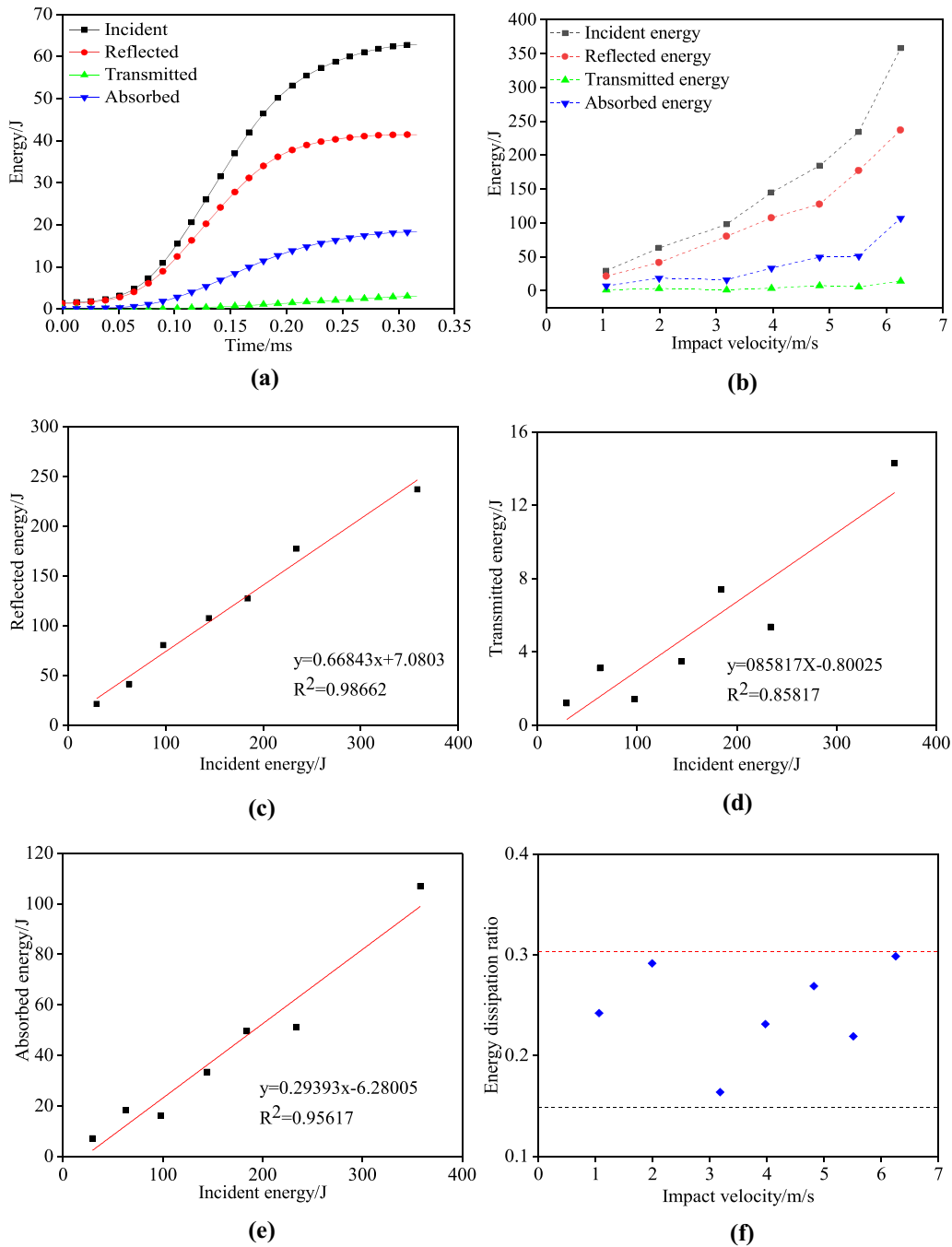
Figure 5. Energy characteristics of coal samples: (**a**) energy change; (**b**) energy at different impact velocities; (**c**) reflected energy; (**d**) transmitted energy; (**e**) reflected energy; (**f**) changes in energy absorption rate.

basically no absorbed energy was produced (Fig. 6a). This stage took very fast, and so it is generally believed that there was almost no compaction stage in the mechanical curve of a coal sample under dy-

namic load. In the initial phases of *BC* and *CD*, a small number of microcracks began to expand in the elastic stage and part of the input energy was dissipated due to the impact load of large energy on the
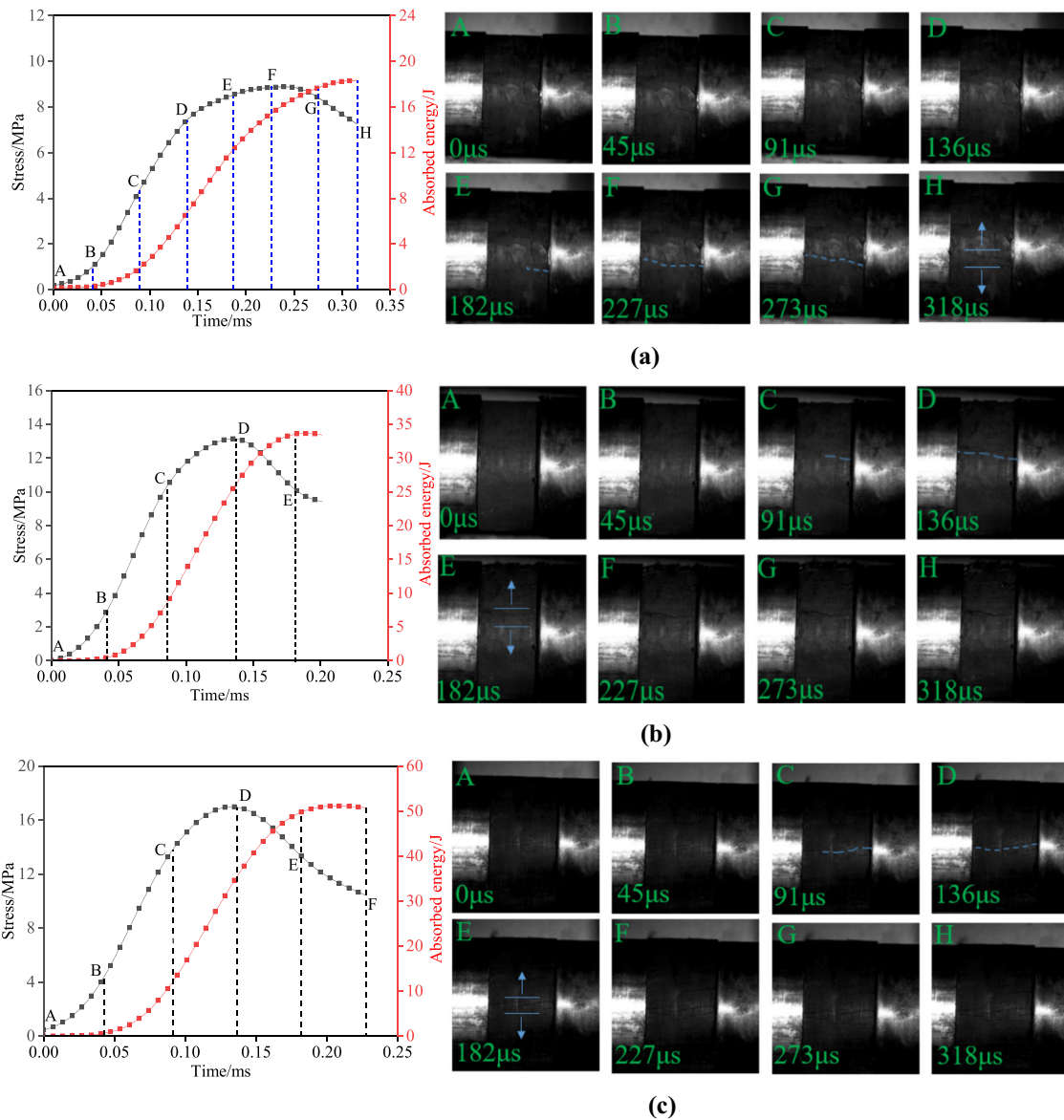
(a)

(b)

(c)

Figure 6. Energy absorption and stress evolution: (**a**) 1.99 m/s; (**b**) 3.97 m/s; (**c**) 4.82 m/s.

coal. The dissipation energy began to increase slowly due to the expansion of local cracks, but the stress rose faster. In the *DE* and *EF* phases, the internal cracks began to initiate, expand and develop in a large area, the coal damage intensified, leading to energy dissipation, and the stress rise rate of coal samples slowed down. As the peak stress was reached, the stress decreased gradually to point *H*. Original and new cracks continued to expand and penetrate. The dissipated energy continued to increase. Finally, the growth rate of dissipated energy

slowed down gradually, and the crushing speed of coal decreased gradually.

In the initial stage of *AB*, dynamic load acted rapidly on the coal sample (Fig. 6b). The coal sample was compacted quickly to produce a small stress, and the corresponding energy was almost 0. With the continuous action of stress wave on the coal sample, the coal sample in *BC* stage was damaged, and the internal cracks were damaged and macro-cracks started to crack gradually. The coal sample at the *CD* stage continued to fracture until it was al-

most completely connected. In the *DE* stage, the peak stress of the coal sample decreased gradually, but the energy was still absorbed along with the crack propagation of the sample. Until the stress of the sample decreased slowly, the bearing capacity of the coal sample further decreased, and the energy absorption stabilized gradually.

The initial action of stress wave on the coal sample in stage *AB* made the internal cracks of the coal sample close (Fig. 6c). The characteristics of this phase were similar to those in Figure 6a and b. With the continuous action of the stress wave, the interior of the *BC* coal sample was damaged and the cracks expanded gradually. Compared with Figure 6a and b, the crack propagation speed became faster. At the *CD* stage, the crack propagation of the coal sample was intensified, and the coal sample showed a failure state when the stress of the sample evolved to the peak stress. In the *DE* stage, the stress of the coal sample decayed gradually, but the crack of the sample was still expanding and still required energy. In the *EF* stage, the stress of the coal sample decreased gradually slowly, and the energy consumption of the coal sample gradually leveled off.

Figure 6 shows clearly that the energy dissipation process of coal failure truly reflects the development rate of coal internal fractures, and it well describes the degree and process of coal failure. At the early stage, the surface cracks continued to expand and failed to penetrate completely when the maximum stress was reached. However, the crack continued to develop and basically expanded axially along the specimen when the maximum stress was reached. In the subsequent stress attenuation process, the surface cracks of coal samples continued to open, accompanied by continuous energy consumption. The stress attenuation after the peak stress does not mean that the energy absorption completely slowed down, which is related to the crushing process of the sample.

By comparing the time–history curve of dissipation energy of coal body in Figure 6a, it was found that there was a linear growth stage of dissipation energy with points *D–F* of dissipation energy. In order to study further the variation law of the steady growth rate of dissipated energy of coal and rock under different impact velocities, the crack propagation coefficient *K* was introduced to better reflect the propagation rate of internal cracks in coal and rock. The *K* value is defined as the slope of the linear fitting curve of the steady growth section of
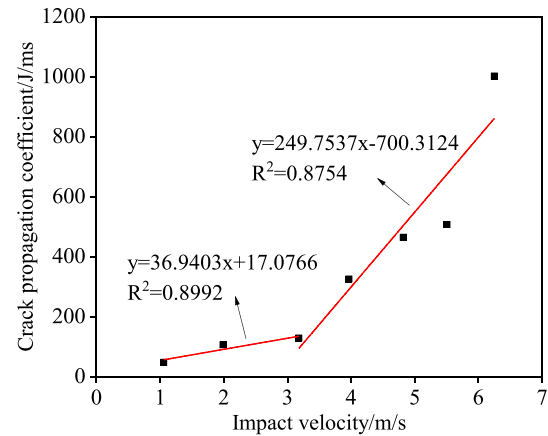

Figure 7. Relationship between dissipation energy growth rate and impact velocity.

the dissipative energy of coal and rock under different impact velocities.

As shown in Figure 7, the *K* value increased linearly with increase in impact velocity. When the impact velocity was 1–3 m/s, the *K* value increased slowly. This indicates that the fracture process of a coal sample is slow when dynamic load is low. When the impact velocity was about 3–6 m/s, the *K* value increased rapidly. Clearly, when the dynamic load is higher, the crack growth rate is faster. Overall, the increase in dynamic load promotes crack propagation.

Combined with Figures 6 and 7, it can be found that the larger the dynamic load is, the sooner the crack propagation time of coal sample will be. The stress evolution process of coal samples is also accelerated.

Coal Fragmentation Characteristics

The particle size distribution of crushed coal samples was characterized quantitatively and the analyzed by collecting crushed coal fragments. Standard screens with specifications of 0–45 mm were used to screen the fragments and weigh the remaining fragments of coal samples on each screen hole. It was converted into the under-screen accumulative percentage of coal sample fragments at each screen size and the accumulative fraction curve of mass percentage of coal sample fragments at different impact velocities was obtained. As shown in Figure 8, when the impact velocity was low, the initial increase rate of particle size percentage was
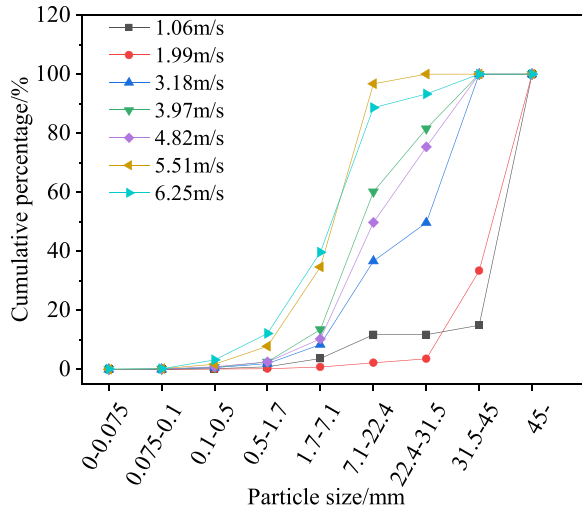
Figure 8. Cumulative mass distribution of broken coal samples.

Figure 9. Coal sample flatness particle size after impact.
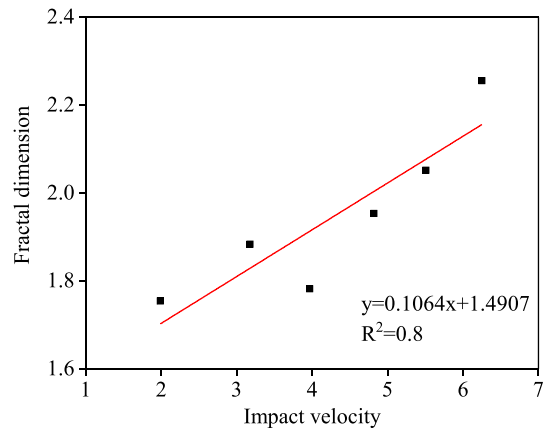
Figure 10. Fractal dimensions of samples at different impact velocities.

slow. The increase rate accelerated and the number of broken samples increased within the particle size range 0–45 mm and when the particle size distribution was 7.1–22.4 mm. When the impact velocity was large, the increase rate of particle size distribution curve was fast at the beginning, but when the particle size range was 7.1–22.4 mm, the increase rate was fast. Clearly, the crushed samples were dominated by massive coarse debris at low velocity, while the crushed samples were dominated by fine debris at high velocity.

The average particle size was calculated according to the quality of the broken sample sieved by each sieve hole (Tian et al., 2023), thus:

$$D = \frac{\sum\limits_{1}^{i} M_i D_i}{M} \qquad (5)$$

where M_i is the mass of fragments screened by two adjacent screens, D_i is the average value of the sieve holes of the two screens, and M is the total mass of fragments.

The average particle size of the broken sample decreased linearly with increase in dynamic load (Fig. 9). According to the crushing form of coal sample in Figure 4, when the impact velocities were 1.06 m/s and 1.99 m/s, the particle size D was 50–60 mm. When the impact velocities were 3.18 m/s, 3.97 m/s and 4.82 m/s, the particle size D was 20–30 mm. When the impact velocities were 5.51 m/s and 6.25 m/s, the particle size D was about 10 mm.
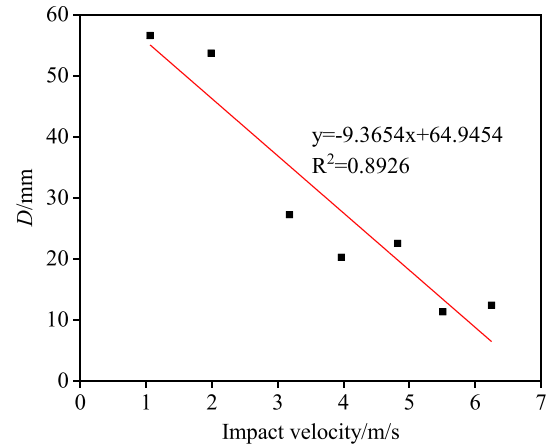
The overall change trend of particle size conforms to the linear relationship: $D = av + b$ ($R^2 \geq 0.89$).

The fractal dimension was calculated according to the specific mass of the fragments under different conditions, and the specific formula of fractal dimension was (Peng et al., 2015; Shen et al., 2022):

$$k = \lg[M(r)/M]/\lg(r) \qquad (6)$$

$$N = 3 - k \qquad (7)$$

where M is the total debris mass, r is the equivalent particle size, namely the screen diameter, $M(r)$ is the mass of debris with sieve diameter less than r, N is the fractal dimension. The calculated values of N by the above methods ranges from 0 to 3. When $0 < N < 2$, the mass proportion of large-scale debris

is larger. When $N = 2$, the proportion of debris mass of each scale is equal. When $2 < N < 3$, the proportion of small scale debris is larger (Peng et al., 2015).

The fractal dimensions of the fragments were about 1.7–2.0 when the impact velocity was less than 5 m/s (Fig. 10), indicating that the broken sample contained chunks, particles and powders. The samples were mainly particles and powders when the impact velocity was higher than 5 m/s, and the degree of breakage of the coal sample intensified gradually. The relationship between N and impact velocity v can be expressed as: $N = av + b$ ($R^2 \geq 0.8$). Fractal dimension values reflect effectively the degree of fracture of coal rock under different strain rates, which has guiding significance in efficient mining of coal mine.

The defects of single coal section such as joint and fissure were developed significantly (Fig. 11). Under the impact load, the coal particles squeezed each other, and the particles formed transgranular or intergranular fracture. The results show that the microcracks in the coal sample were constantly friction and expansion in the process of dynamic load impact. The damage behavior of coal mass caused by stress wave was analyzed based on microscopic and high-speed photographic images of coal sample failure. When the stress wave was in contact with the crack, it was reflected as tensile wave on the crack surface and drove crack propagation (Wang et al., 2021b, 2021c). The higher the impact velocity, the greater the stress wave acting on the coal sample. Due to the dynamic load stress wave in a short period of time and continuous action with coal samples, a stress concentration zone was formed at the crack tip inside the coal sample, and failure occurred due to the limited plastic deformation that the tip can withstand (Wang et al., 2021c). Based on Figures 6 and 11, the dynamic failure process of coal sample was accompanied by the expansion of original cracks and the generation of new cracks.

Critical Strain Rate Analysis

The process of coal sample failure under the action of stress wave is also a process of energy accumulation (Fig. 12). The mechanical strength variation, energy evolution and fracture characteristics of coal under stress wave were significantly correlated, and the dynamic load was highly af-

fected. When the stress wave acted on the coal sample along the pressure bar, the coal body deformation generated the force gradually. Due to the damage caused by the stress and deformation of the sample, energy consumption was generated gradually. At this stage, the energy consumption increased gradually until it became stable, while the stress increased first and then decreased. Finally, the sample could no longer bear the stress and the energy consumption became stable gradually.

The specimens also showed various macroscopic failure forms, which were related to different strain rates. When the strain rate was small (0–20/s^{-1}), there was almost no damage to the coal sample, and only dynamic stress waves constantly acted on the coal sample. At this time, the dynamic strength was small and the sample had almost no deformation, which can be called vibration load. With gradual increase in strain rate, when the strain rate was about 20–40/s^{-1}, the coal sample deformed and fractured; however, the overall outline of the coal sample was clearly visible. The sample was based on a large semicircular cake. At this stage, when the stress wave acted on the coal sample, the crack on the coal sample surface continued to expand until it cracked. When the strain rate continued to increase (40–80/s^{-1}), the damage degree of coal sample was aggravated. In addition to the generation of a large number of cracks, a large number of small scale fragments was generated in the coal samples, and the energy consumption of coal samples continued to increase. When the strain rate was 80–120/s^{-1}, the crushing degree of coal sample was more aggravated, and a lot of powder particles appeared. Clearly, there were critical strain rates of 20/s^{-1}, 40/s^{-1} and 80/s^{-1} under dynamic loading of coal samples in this study. The coal under the action of stress wave had experienced the process from no damage, fracture, crushing and severe crushing. The dynamic strength of the coal sample increased gradually, and the energy of failure process increased gradually.

MECHANICAL CONSTITUTIVE MODEL OF COAL SAMPLE AND ITS VERIFICATION

Model Building

The mechanical constitutive model of coal sample can describe its strength and deformation characteristics well, providing a theoretical basis for
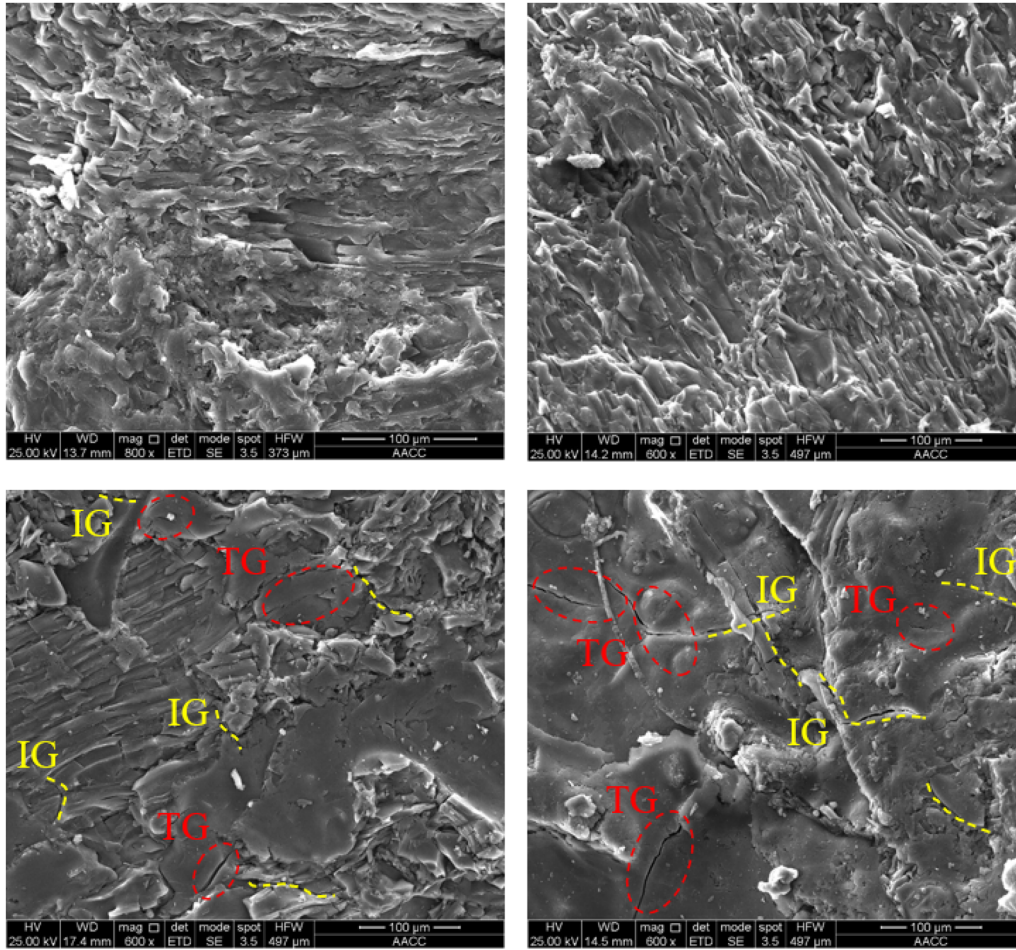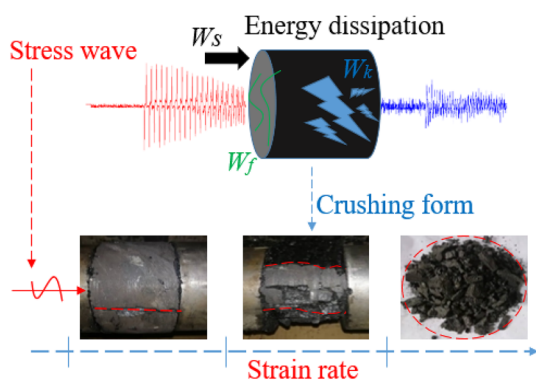
Figure 11. Microscopic fracturing modes of coal.

Figure 12. Schematic diagram of coal impact evolution.

engineering practice and numerical simulation. Assuming that coal element strength follows the

Weibull distribution, this probability density function $P(F)$ can be expressed as (Kong et al., 2021; Li et al., 2023b):

$$P(F) = \frac{c}{F_0} \left(\frac{F}{F_0}\right)^{c-1} \exp\left[-\left(\frac{F}{F_0}\right)^c\right] \quad (8)$$

where F, c and F_0 are the distribution variables and distribution parameters of the cell body, respectively. Aiming at the above assumptions, the damage variable D is introduced and expressed as:

$$D = \frac{N_f}{N} \quad (9)$$

where N_f is the number of destroyed elements under a certain load, and N is the total number of units. The number of destroyed particles in any interval $[F,$

$F + dF]$ is $NP(x)dx$. Therefore, the number of destructive elements can be expressed as:

$$N_f(F) = \int_0^F NP(x)dx = N\left\{1 - \exp\left[-\left(\frac{F}{F_0}\right)^c\right]\right\}$$
(10)

Equation 11 is substituted into Eq. 10 to simplify, thus:

$$D = 1 - \exp\left[-\left(\frac{F}{F_0}\right)^c\right]$$
(11)

Considering the influence of intermediate principal stress in D–P criterion measurement (Amstutz et al., 2012), the strength criterion of coal body is:

$$F = f(\sigma) = \alpha_0 I_1 + \sqrt{J_2}$$
(12)

where α_0 is the test constant. The expression formula of each indicator is, respectively (Lu et al., 2021):

$$\alpha_0 = \frac{\sin\varphi}{\sqrt{3(3 + \sin^2\varphi)}}$$
(13)

$$I_1 = \frac{(\sigma_1 + 2\sigma_3)E\varepsilon_1}{(\sigma_1 - 2\mu\sigma_3)}$$
(14)

$$\sqrt{J_2} = \frac{(\sigma_1 - \sigma_3)E\varepsilon_1}{\sqrt{3}(\sigma_1 - 2\mu\sigma_3)}$$
(15)

where φ is the average value (30°). Considering the forces acting on coal sample $\sigma_2 = \sigma_3 = 0$ MPa, the expression of cell strength is:

$$F = \left(\alpha + \frac{1}{\sqrt{3}}\right)E\varepsilon$$
(16)

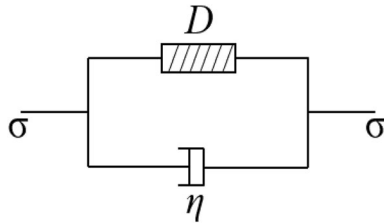The strain rate effect should be considered in the constitutive relation of coal. Referring to relevant literature, the Kelvin model was adopted to improve the aging damage model of coal (Li et al., 2015; Shan et al., 2018), as shown in Figure 13.

The constitutive relation of the viscous body is (Shan et al., 2019):

$$\sigma_b = \eta \cdot \frac{d\varepsilon}{dt}$$
(17)

where η is the coal viscosity coefficient, which ranges from 0 to 0.5 (Yin et al., 2018; Wang et al., 2022).

According to the equivalent strain hypothesis, the constitutive relation of the damaged body can be written as:

$$\sigma_a = E\varepsilon(1 - D) = E\varepsilon\exp\left[-\left(\frac{F}{F_0}\right)^c\right]$$
(18)

According to Eqs. 17 and 18, the following relation can be obtained:

$$\sigma = E\varepsilon(1 - D) = E\varepsilon\exp\left[-\left(\frac{F}{F_0}\right)^c\right] + \eta \cdot \frac{d\varepsilon}{dt}$$
(19)

Because the combined force of dynamic (σ_d) and static (σ_s) loads can be provided along the impact direction, the following expression is defined:

$$\sigma_d = \sigma - \sigma_s$$
(20)

By combining Eqs. 19 and 20, the kinetic model of a coal sample can be obtained as:

$$\sigma_d = E\varepsilon\exp\left[-\left(\frac{F}{F_0}\right)^c\right] - \sigma_s + \eta \cdot \frac{d\varepsilon}{dt}$$
(21)

It can be seen from Eq. 21 that model parameters F_0 and c need to be determined to establish the constitutive model. From the multivariate function for solving the extreme value problem, it can be seen that at point (σ_m, ε_m) of the curve (Kong et al., 2021), there is:

$$\left.\frac{d\sigma}{d\varepsilon}\right|(\sigma_m,\ \varepsilon_m) = 0$$
(22)

By combining Eqs. 21 and 22, the following can be obtained:

$$F_0 = \left(\alpha_0 + \frac{1}{\sqrt{3}}\right)E\varepsilon_m \cdot c^{\frac{1}{c}}$$
(23)

$$c = \frac{1}{\ln(E\varepsilon_m) - \ln\left(\sigma_m + \sigma_s - \eta \cdot \frac{d\varepsilon}{dt}\right)}$$
(24)

Figure 13. Damage model of coal sample..

According to Eqs. 21, 23 and 24, the mechanical constitutive model of coal sample can be obtained as:

$$\sigma_d = E\varepsilon \exp\left[-\left(\frac{\left(\alpha + \frac{1}{\sqrt{3}}\right)E\varepsilon}{\left(\alpha_0 + \frac{1}{\sqrt{3}}\right)E\varepsilon_m \cdot c_c^{\frac{1}{c}}}\right)^{\overline{\ln(E\varepsilon_m) - \ln\left(\sigma_m + \sigma_s - \eta\frac{d\varepsilon}{dt}\right)}}\right] - \sigma_s + \eta \cdot \frac{d\varepsilon}{dt}$$

(25)

According to Eqs. 23 and 25, the following can be obtained by simplifying:

$$\sigma_d = E\varepsilon \exp\left\{-\left(\frac{\varepsilon}{\varepsilon_m}\right)^{\overline{\ln(E\varepsilon_m) - \ln\left(\sigma_m + \sigma_s - \eta\cdot\frac{d\varepsilon}{dt}\right)}} \cdot [\ln(E\varepsilon_m) - \ln\left(\sigma_m + \sigma_s - \eta\cdot\frac{d\varepsilon}{dt}\right)]\right\} - \sigma_s + \eta\cdot\frac{d\varepsilon}{dt}$$

(26)

Equation 26 shows the combined action of static prestress and dynamic stress wave on coal samples. Considering that $\sigma_s = 0$ MPa in this experiment, Eq. 26 can be simplified as:

$$\sigma_d = E\varepsilon \exp\left\{-\left(\frac{\varepsilon}{\varepsilon_m}\right)^{\overline{\ln(E\varepsilon_m) - \ln\left(\sigma_m - \eta\frac{d\varepsilon}{dt}\right)}} \cdot [\ln(E\varepsilon_m) - \ln\left(\sigma_m - \eta\cdot\frac{d\varepsilon}{dt}\right)]\right\} + \eta\cdot\frac{d\varepsilon}{dt}$$

(27)

The above model was used to calculate the stress. Figure 14 shows an example of the mechanical curve under different velocities. The curve of theoretical calculation and the curve of experimental measurement show basically the same trend.

Damage Evolution Process

According to Eqs. 11 and 23, it can be deduced that the exit damage D is:

$$D = 1 - \exp\left[-\left(\frac{\varepsilon}{\varepsilon_m}\right)^c \cdot \frac{1}{c}\right]$$

(28)

By combining Eqs. 23 and 28, D can be expressed as:

$$D = 1 - exp\left\{-\left(\frac{\varepsilon}{\varepsilon_m}\right)^{\overline{\ln(E\varepsilon_m) - \ln\left(\sigma_m - \eta\frac{d\varepsilon}{dt}\right)}} \cdot \left[\ln(E\varepsilon_m) - \ln\left(\sigma_m - \eta\cdot\frac{d\varepsilon}{dt}\right)\right]\right\}$$

(29)

The damage variable increased gradually with increase in strain Fig. 15). When the impact velocity was small (v = 3.18 m/s), the damage variable rose slowly at first. However, the damage quantity increased rapidly in the initial damage stage with increase in impact velocity (v = 3.97, 4.82, 6.25 m/s). In the stress plastic deformation stage, the damage changes of coal samples were approximately linear. Damage changes slowed down slightly after the post-peak stage of mechanical curve of coal sample. This indicates that it was still in deformation and failure after the coal sample was broken. This also shows that energy absorption can increase even after the maximum stress (Fig. 6).

It is clear from the damage changes of coal samples at the above four speeds that the increase of dynamic load promoted the fracture of coal samples. This is corresponds to the conclusion analyzed in Figure 7. In addition, the variation trend of the maximum damage quantity is also related to energy and crushing. The more severe the damage degree of coal sample was under the action of high stress wave, the maximum damage amount increased gradually. In addition, the dynamic damage evolution curve of coal sample increased faster than that of rock and concrete by comparing related studies on rocks (Zhu et al., 2012; Yin et al., 2018) and concrete (Tan et al., 2022). The initial damage evolution stage of rock and concrete shows a downward convex trend, while this phenomenon is almost not obvious in coal. This may be related to the density of rock and concrete materials, internal crack development degree, porosity size and so on. Coal samples are more prone to damage and destruction under the action of stress waves.

CONCLUSIONS

Part of the energy is still absorbed when the peak stress decays due to the continuous fracture of coal sample under uniaxial impact load. The absorbed energy of coal shows a process from slow to fast and then from slow to stable at different stress stages. And the increase of dynamic load also increases the crack propagation speed to some extent.

Coal fragments have good fractal characteristics. Combined with the high-speed camera shooting and SEM characteristic analysis of coal sample, the crack of coal sample shows tensile failure. The failure of coal samples under dynamic load corresponds to the critical strain rate. The strain rate increases gradually, and the coal samples show the states of intact, broken, and (complete) failure successively.
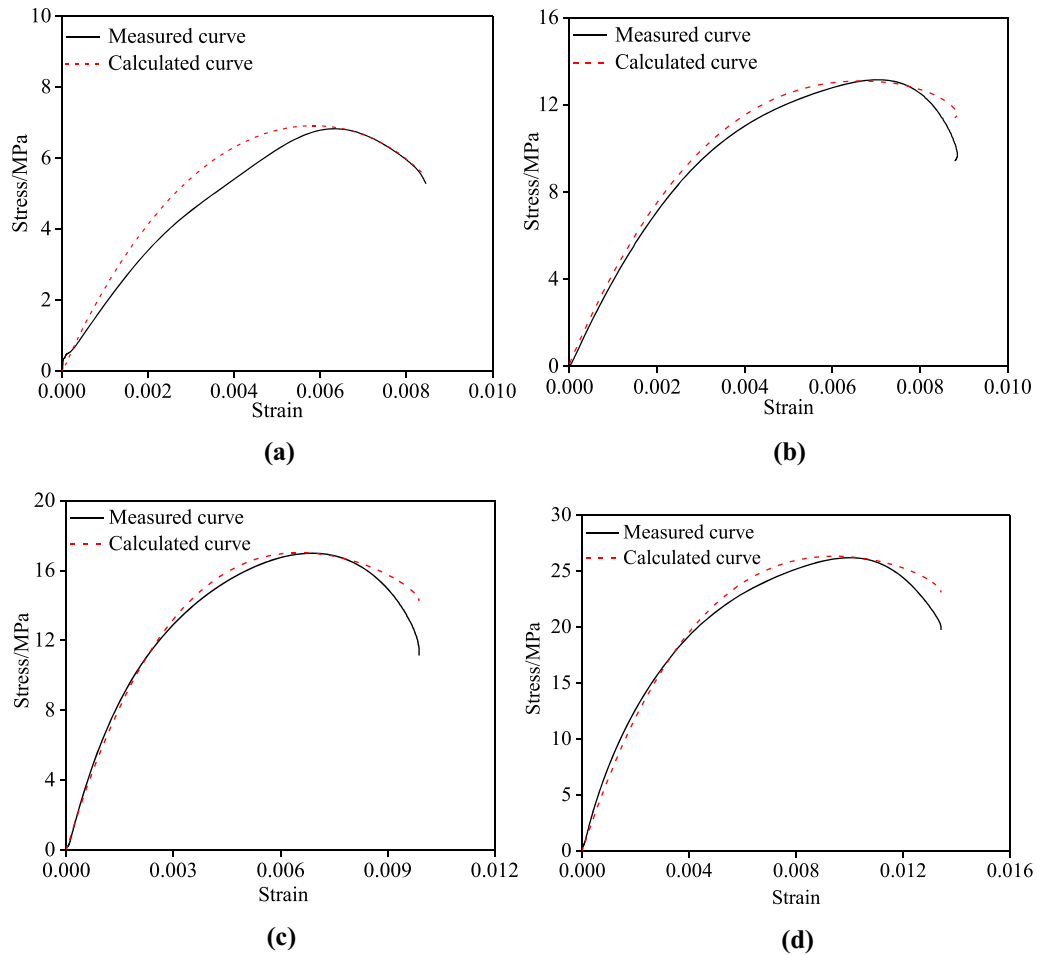
Figure 14. Fitting and experimental stress–strain curves for different velocities: (**a**) 3.18 m/s; (**b**) 3.97 m/s; (**c**) 4.82 m/s; (**d**) 6.25 m/s.

Considering the strain rate, the mechanical constitutive model of coal samples under dynamic load is established, and the damage variation of coal samples under dynamic load is analyzed. The model reflects the stress evolution of coal samples well.

The larger of the failure strength of coal will cause the higher of absorption energy and the larger of the sample fractal dimension. Coal strength under impact load can be used as dynamic load resistance index to reflect the strength of dynamic load resistance. The fractal dimension of debris can be used as dynamic load impact energy index to measure the severity of dynamic load impact damage.
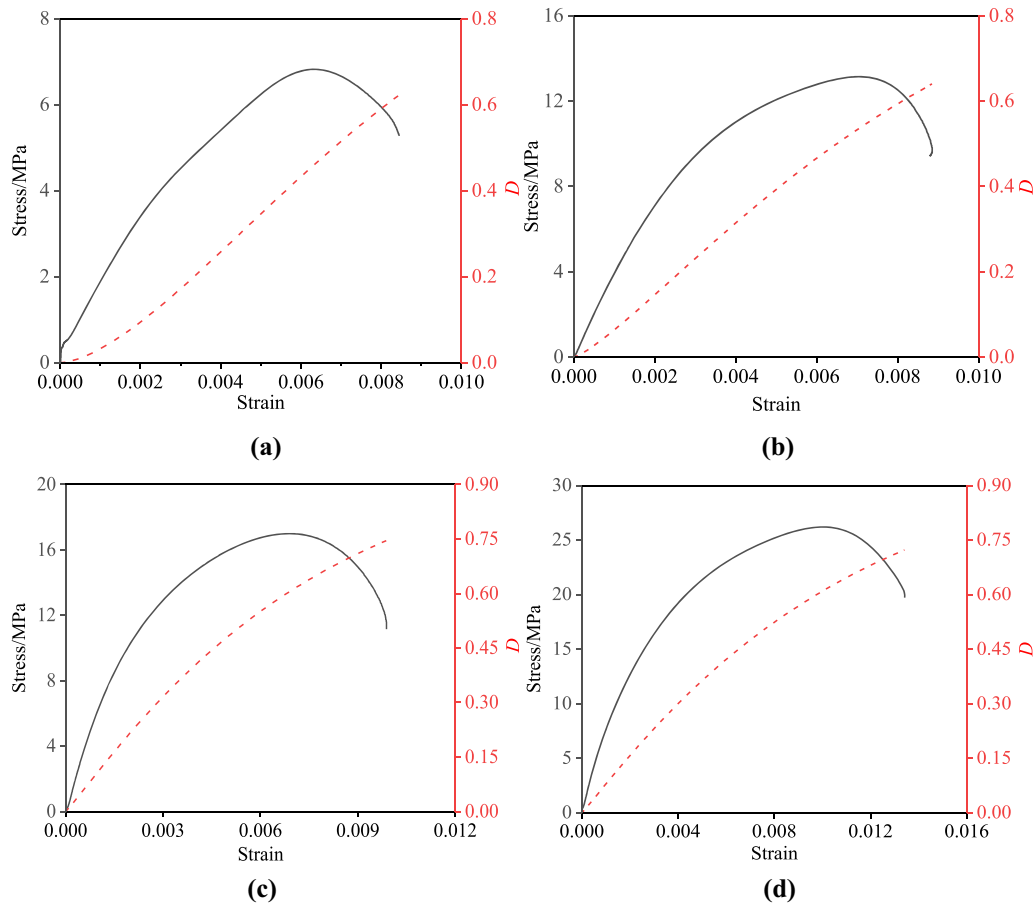
Figure 15. Stress and damage evolution curves under different velocities: (**a**) 3.18 m/s; (**b**) 3.97 m/s; (**c**) 4.82 m/s; (**d**) 6.25 m/s.

REFERENCES

Ai, D. H., Zhao, Y. C., Wang, Q. F., & Li, C. W. (2019). Experimental and numerical investigation of crack propagation and dynamic properties of rock in SHPB indirect tension test. *International Journal of Impact Engineering, 126*, 135–146.

Amstutz, S., Novotny, A. A., & Neto, E. A. D. (2012). Topological derivative-based topology optimization of structures subject to Drucker-Prager stress constraints. *Computer Methods in Applied Mechanics and Engineering, 233*, 123–136.

Ding, Z., Feng, X. J., Wang, E. Y., Wei, Q. L., Zhao, X., & Hu, Q. J. (2023). Acoustic emission response and evolution of pre-

cracked coal in the meta-instability stage under graded loading. *Engineering Geology, 312*, 106930. https://doi.org/10.1016/j.enggeo.2022.106930.

Fairhurst, C. (2017). Some challenges of deep mining. *Engineering, 3*(4), 527–537.

Feng, J. J., Wang, E. Y., Chen, X., & Ding, H. C. (2018). Energy dissipation rate: An indicator of coal deformation and failure under static and dynamic compressive loads. *International Journal of Mining Science and Technology, 28*(3), 397–406.

Feng, J. J., Wang, E. Y., Huang, Q. S., Ding, H. C., & Zhang, X. Y. (2020). Experimental and numerical study of failure behavior and mechanism of coal under dynamic compressive loads. *International Journal of Mining Science and Technology, 30*(5), 613–621.

Feng, J. J., Wang, E. Y., Shen, R. X., Chen, L., Li, X. L., & Xu, Z. Y. (2016). Investigation on energy dissipation and its mechanism of coal under dynamic loads. *Geomechanics and Engineering, 11*(5), 657–670.

Feng, X. J., Ding, Z., Ju, Y. Q., Zhang, Q. M., & Ali, M. (2022). "Double peak" of dynamic strengths and acoustic emission responses of coal masses under dynamic loading. *Natural Resources Research, 31*(3), 1705–1720.

Gu, Z. J., Shen, R. X., Liu, Z. T., Zhao, E. L., Chen, H. L., Yuan, Z. C., & Tian, J. W. (2023). Dynamic characteristics of coal under triaxial constraints based on the split-hopkinson pressure bar test system. *Natural Resources Research, 32*(2), 587–601.

Hao, X. J., Du, W. S., Zhao, Y. X., Sun, Z. W., Zhang, Q., Wang, S. H., & Qiao, H. Q. (2020). Dynamic tensile behaviour and crack propagation of coal under coupled static-dynamic loading. *International Journal of Mining Science and Technology, 30*(5), 659–668.

Ju, Y., Sudak, L., & Xie, H. P. (2007). Study on stress wave propagation in fractured rocks with fractal joint surfaces. *International Journal of Solids and Structures, 44*(13), 4256–4271.

Kaiser, P. K., & Kim, B. H. (2015). Characterization of strength of intact brittle rock considering confinement-dependent failure processes. *Rock Mechanics and Rock Engineering, 48*(1), 107–119.

Kong, X. G., He, D., Liu, X. F., Wang, E. Y., Li, S. G., Liu, T., & Yang, S. R. (2022). Strain characteristics and energy dissipation laws of gas-bearing coal during impact fracture process. *Energy, 242*, 123028.

Kong, X. G., Li, S. G., Wang, E. Y., Ji, P. F., Wang, X., Shuang, H. Q., & Zhou, Y. X. (2021). Dynamics behaviour of gas-bearing coal subjected to SHPB tests. *Composite Structures, 256*, 113088.

Li, C. J., Xu, Y., Chen, P. Y., Li, H. L., & Lou, P. J. (2020a). Dynamic mechanical properties and fragment fractal characteristics of fractured coal-rock-like combined bodies in split hopkinson pressure bar tests. *Natural Resources Research, 29*(5), 3179–3195.

Li, H. R., Qiao, Y. F., He, M. C., Shen, R. X., Gu, Z. J., Cheng, T., & Tang, J. (2023b). Effect of water saturation on dynamic behavior of sandstone after wetting-drying cycles. *Engineering Geology, 319*, 107105. https://doi.org/10.1016/j.enggeo.2023.107105.

Li, M. M., Liang, W. M., & Yue, G. W. (2020b). Fractal and pore structure analysis of structural anisotropic coal under different impact loads. *Environmental Earth Sciences, 79*(13), 323.

Li, X. B., Gu, H. L., Tao, M., Peng, K., Cao, W. Z., & Li, Q. Y. (2021b). Failure characteristics and meso-deterioration mechanism of pre-stressed coal subjected to different dynamic loads. *Theoretical and Applied Fracture Mechanics, 115*, 103061.

Li, X. L., Liu, Z. T., Feng, X. J., Zhang, H. J., & Feng, J. J. (2021a). Effects of acid sulfate and chloride ion on the pore structure and mechanical properties of sandstone under dynamic loading. *Rock Mechanics and Rock Engineering, 54*(12), 6105–6121.

Li, X., Liu, Z., Zhao, E., Liu, Y., Feng, X., & Gu, Z. (2023a). Experimental study on the damage evolution behavior of coal under dynamic Brazilian splitting tests based on the split Hopkinson pressure bar and the digital image correlation. *Natural Resources Research, 32*(3), 1435–1457.

Li, X. B., Wang, S. M., Weng, L., Huang, L. Q., Zhou, T., & Zhou, J. (2015). Damage constitutive model of different age concretes under impact load. *Journal of Central South University, 22*(2), 693–700.

Li, X. B., Zhou, Z. L., Lok, T. S., Hong, L., & Yin, T. B. (2008). Innovative testing technique of rock subjected to coupled static and dynamic loads. *International Journal of Rock Mechanics and Mining Sciences, 45*(5), 739–748.

Liu, X. H., Dai, F., Zhang, R., & Liu, J. F. (2015). Static and dynamic uniaxial compression tests on coal rock considering the bedding directivity. *Environmental Earth Sciences, 73*(10), 5933–5949.

Liu, Y. B., Yin, G. Z., Li, M. H., Zhang, D. M., Deng, B. Z., Liu, C., & Lu, J. (2019). Anisotropic mechanical properties and the permeability evolution of cubic coal under true triaxial stress paths. *Rock Mechanics and Rock Engineering, 52*(8), 2505–2521.

Lu, W. B., Zhu, Z. D., He, Y. X., & Que, X. C. (2021). Strength characteristics and failure mechanism of a columnar jointed rock mass under uniaxial, triaxial, and true triaxial confinement. *Rock Mechanics and Rock Engineering, 54*(5), 2425–2439.

Ma, S. S., Chen, W. Z., & Zhao, W. S. (2021). Effects of axial static stress and confining pressure on the dynamic compressive behaviours of granite. *European Journal of Environmental and Civil Engineering, 25*(5), 795–812.

Peng, R. D., Ju, Y., Wang, J. G., Xie, H. P., Gao, F., & Mao, L. T. (2015). Energy dissipation and release during coal failure under conventional triaxial compression. *Rock Mechanics and Rock Engineering, 48*(2), 509–526.

Shan, R. L., Song, Y. W., Song, L. W., & Bai, Y. (2019). Dynamic property tests of frozen red sandstone using a split Hopkinson pressure bar. *Earthquake Engineering & Engineering Vibration, 18*(3), 511–519.

Shan, R. L., Song, Y. W., Song, L. W., Huang, P. C., Dai, X., & Zhou, T. (2018). Time dependent damage model of northwest artificial frozen red sandstone under dynamic loading. *Journal of China Coal Society, 43*(1), 118–123.

Shen, X., Shen, Y., Xu, J. H., & Liu, H. L. (2022). Influence of the fractal distribution of particle size on the critical state characteristics of calcareous sand. *Fractal and Fractional, 6*(3), 165.

Tan, Y. Z., Shi, X. M., Cheng, Y. H., Li, G., Yue, S. L., Wang, M. Y., & Zhou, J. W. (2022). Research on the damage evolution law and dynamic damage constitutive model of high-performance equal-sized-aggregate concrete materials. *Journal of Materials in Civil Engineering, 34*(5), 04022039.

Tian, H., Li, Z. H., Yin, S., Lei, Y. Y., Niu, Y., Wang, X. Y., Zang, Z. S., & Gu, Z. J. (2023). Research on infrared radiation response and energy dissipation characteristics of sandstone crushing under impact load. *Engineering Geology, 322*, 107171.

Wang, P., Xu, J. Y., Liu, S. H., & Wang, H. Y. (2016). Dynamic mechanical properties and deterioration of red-sandstone subjected to repeated thermal shocks. *Engineering Geology, 212*, 44–52.

Wang, F., Wang, H. B., Xu, Y., Cheng, B., & Wang, Q. Q. (2021a). Analysis of energy dissipation characteristics of damaged sandstone under impact load. *Shock and Vibration, 2021*, 1–10.

Wang, X. R., Asem, P., Hu, C., & Labuz, J. F. (2021b). Microcracking in tensile fracture of a brittle rock. *Engineering Fracture Mechanics, 251*, 107789.

Wang, X. R., Wang, E. Y., Liu, X. F., & Zhou, X. (2021c). Failure mechanism of fractured rock and associated acoustic behaviors under different loading rates. *Engineering Fracture Mechanics, 247*, 107674.

Wang, D. M., Wang, E. Y., Feng, X. J., Wei, M. Y., Li, D. X., Liu, Q. L., & Zhang, X. (2022). Triaxial creep damage-catastrophe instability characteristics and a nonlinear constitutive model of gas-bearing coal. *Bulletin of Engineering Geology and the Environment, 81*(10), 437.

Xie, H. P., Gao, M. Z., Zhang, R., Peng, G. Y., Wang, W. Y., & Li, A. Q. (2019). Study on the mechanical properties and mechanical response of coal mining at 1000m or deeper. *Rock Mechanics and Rock Engineering, 52*(5), 1475–1490.

Xie, H. P., Li, C., He, Z. Q., Li, C. B., Lu, Y. Q., Zhang, R., & Gao, F. (2021). Experimental study on rock mechanical behavior retaining the in situ geological conditions at different depths. *International Journal of Rock Mechanics and Mining Sciences, 138*, 104548.

Yang, Z. H., Fan, C. J., Lan, T. W., Li, S., Wang, G. F., Luo, M. K., & Zhang, H. W. (2019). Dynamic mechanical and microstructural properties of outburst-prone coal based on compressive SHPB tests. *Energies, 12*(22), 4236.

Yao, W., He, T. M., & Xia, K. W. (2017). Dynamic mechanical behaviors of Fangshan marble. *Journal of Rock Mechanics and Geotechnical Engineering, 9*(5), 807–817.

Yin, T. B., Wang, P., Yang, J., & Li, X. B. (2018). Mechanical behaviors and damage constitutive model of thermally treated sandstone under impact loading. *IEEE Access, 6*, 72047–72062.

Zang, Z. S., Li, Z. H., Niu, Y., Tian, H., Zhang, X., Li, X. L., & Ali, M. (2021). Energy dissipation and electromagnetic radiation response of sandstone samples with a pre-existing crack of various inclinations under an Impact load. *Minerals, 11*(12), 1363.

Zhang, H. W., Wan, Z. J., Ma, D., Zhang, Y., Cheng, J. Y., & Zhang, Q. (2017). Experimental investigation on the strength and failure behavior of coal and synthetic materials under plane-strain biaxial compression. *Energies, 10*(4), 500.

Zhao, Y. X., Zhao, G. F., Jiang, Y. D., Elsworth, D., & Huang, Y. Q. (2014). Effects of bedding on the dynamic indirect tensile strength of coal: Laboratory experiments and numerical simulation. *International Journal of Coal Geology, 132*, 81–93.

Zhou, X., Liu, X. F., Wang, X. R., Liu, Y. B., Xie, H., & Du, P. F. (2023). Acoustic emission characteristics of coal failure under triaxial loading and unloading disturbance. *Rock Mechanics and Rock Engineering, 56*(2), 1043–1061.

Zhu, J. J., Li, X. B., Gong, F. Q., Wang, S. M., & He, W. (2012). Experimental test and damage characteristics of sandstone under uniaxial impact compressive loads. *Journal of Central South University, 43*(7), 2701–2707.